Accepted Manuscript

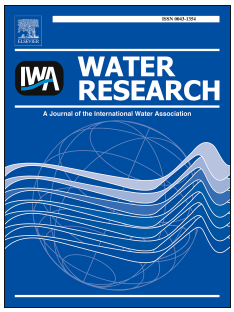

Self similarities in desalination dynamics and performance using capacitive deionization

Ashwin Ramachandran, Ali Hemmatifar, Steven A. Hawks, Michael Stadermann, Juan G. Santiago

PII: S0043-1354(18)30336-1

DOI: 10.1016/j.watres.2018.04.042

Reference: WR 13739

To appear in: *Water Research*

Received Date: 6 February 2018

Revised Date: 16 April 2018

Accepted Date: 17 April 2018

Please cite this article as: Ramachandran, A., Hemmatifar, A., Hawks, S.A., Stadermann, M., Santiago, J.G., Self similarities in desalination dynamics and performance using capacitive deionization, *Water Research* (2018), doi: 10.1016/j.watres.2018.04.042.

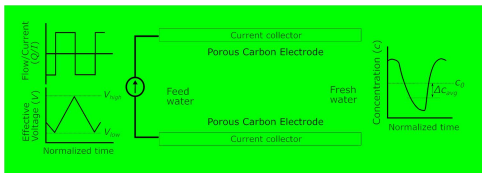

Self similarities in desalination dynamics and performance using capacitive deionization

Ashwin Ramachandran [a], Ali Hemmatifar [b], Steven A. Hawks [c], Michael Stadermann [c], Juan G. Santiago [b,*]

[a] Department of Aeronautics & Astronautics, Stanford University, Stanford, California 94305, United States

[b] Department of Mechanical Engineering, Stanford University, Stanford, California 94305, United States

[c] Lawrence Livermore National Laboratory, 7000 East Avenue, Livermore, California 94550, United States

* To whom correspondence should be addressed. Tel. 650-736-1283, Fax 650-723-7657, E-mail: juan.santiago@stanford.edu

Abstract

Charge transfer and mass transport are two underlying mechanisms which are coupled in desalination dynamics using capacitive deionization (CDI). We developed simple reduced-order models based on a mixed reactor volume principle which capture coupled dynamics of CDI operation using closed-form semi-analytical and analytical solutions. We use the models to identify and explore self-similarities in the dynamics among flow rate, current, and voltage for CDI cell operation including both charging and discharging cycles. The similarity approach identifies the specific combination of cell (e.g. capacitance, resistance) and operational parameters (e.g. flow rate, current) which determine a unique effluent dynamic response. We here demonstrate self-similarity using a conventional flow between CDI (fbCDI) architecture, and we hypothesize that our similarity approach has potential application to a wide range of designs. We performed an experimental study of these dynamics and used well-controlled experiments of CDI cell operation to validate and explore limits of the model. For experiments,

we used a CDI cell with five electrode pairs and a standard flow between (electrodes) architecture. Guided by the model, we performed a series of experiments that demonstrate natural response of the CDI system. We also identify cell parameters and operation conditions which lead to self-similar dynamics under a constant current forcing function and perform a series of experiments by varying flowrate, currents, and voltage thresholds to demonstrate self-similarity. Based on this study, we hypothesize that the average differential electric double layer (EDL) efficiency (a measure of ion adsorption rate to EDL charging rate) is mainly dependent on user-defined voltage thresholds, whereas flow efficiency (measure of salt deficit or enrichment at effluent) depends on cell volumes flowed during charging, which is determined by flowrate, current and voltage thresholds. Results of experiments strongly support this hypothesis. Results show that cycle efficiency and salt removal for a given flowrate and current are maximum when average EDL and flow efficiencies are approximately equal. We further explored a range of CC operations with varying flowrates, currents, and voltage thresholds using our similarity variables to highlight trade-offs among salt removal, energy, and throughput performance.

Keywords: Capacitive deionization, water desalination, reduced order model, self-similarity, porous carbon electrodes, performance optimization

1. Introduction

Capacitive deionization (CDI) is an emerging desalination technology that has potential to efficiently treat brackish water (salt content of 1 to 10 g/L) (Oren, 2008; Suss et al., 2015). In CDI, the ions in solution are sequestered into electric double layers within the porous electrodes leaving water with lower salt content to be flushed from the cell. CDI performance is known to be significantly affected by operating conditions such as source voltage/current, electrode

dimensions, cell resistance and capacitance, flowrate, and feed concentration (Kim and Yoon, 2014; Wang and Lin, 2018; R Zhao et al., 2013a; R Zhao et al., 2013b).

CDI electrical charging results in simultaneous adsorption of counter-ions and desorption of co-ions (Avraham et al., 2009). Hence, dynamics associated with electric double layer (EDL) charge efficiency plays an important role in salt removal and regeneration using CDI (Zhao et al., 2010). Biesheuvel et al. (2009) developed a dynamic model for CDI to predict desalination dynamics using both Gouy Chapmann Stern (GCS) theory and a mixed flow reactor model for salt removal, and the study validated the model, including effluent salt dynamics, with constant voltage (CV) operation experiments. Subsequently, Biesheuvel and Bazant (2010) developed a non-linear mean-field theory for capacitive charging and discharging using ideal porous electrodes, and identified limiting time scales in CDI desalination dynamics. Biesheuvel and Bazant (2010) described the importance of operation in the desalination regime corresponding to large voltages (compared to the thermal voltage) for achieving practical amounts of salt removal, thus highlighting the role of careful choice of voltage limits for desalination. Jande and Kim (2013) developed a simple dynamic response model with analytical solutions to describe time variation of effluent concentration under constant current (CC) charging. However, Jande and Kim (2013) neglected dynamics associated with EDLs, which was shown to play an important role in desalination as highlighted in earlier works (Biesheuvel et al. (2009); Zhao et al., 2010). Later, Hemmatifar et al. (2015) developed a high fidelity two-dimensional porous electrode model for flow between CDI (fbCDI) which was solved computationally and validated experimentally. Hemmatifar et al. (2015) highlighted several underlying physical mechanisms including depletion in electrodes and diffusion in spacer within the CDI cell during electrical charging and discharging. Similar modeling efforts have recently been carried out for flow-

through electrode (fteCDI) CDI systems. Guyes et al. (2017) developed a simple one-dimensional model for an fteCDI architecture, and highlighted the importance of developing simple engineering models for CDI operation. In addition, a recent work (Qu et al., 2018a) on fteCDI used a hierarchy of simple to complex models to study the interplay between charging and transport dynamics in CDI**.**

Most existing models and analyses for CDI discussed earlier have been either overly simple (e.g., neglecting EDL dynamics, considering only charging phase, or not involving dynamic steady state conditions) or overly complex in scope to clearly highlight general scaling and self-similar behavior. For example, mixed reactor models assuming a constant EDL efficiency irrespective of operation (Jande and Kim, 2013) or which do not separate the effects of flow efficiency and EDL efficiency (Biesheuvel et al., 2009), do not capture the underlying trade-offs in desalination performance when operated with varying values of flowrate to current ratio and voltage windows (two of the parameters leading to similarity highlighted in our work). More comprehensive models such as the numerical two-dimensional fbCDI model of Hemmatifar et al., 2015, and the one-dimensional fteCDI model of Guyes et al., 2017 enable greater (and perhaps higher fidelity) spatiotemporal information, but these are difficult to probe to clearly identify key parameters describing the trade-offs among desalination depth, energy, and throughput in CDI.

Here, we aim to capture the essential governing dynamics and identify controllable parameters for tuning desalination performance using CDI. We focus our study on CC charge-discharge operation since it is energy efficient (Kang et al., 2014; Qu et al., 2016) and has better energy recovery (Han et al., 2015; Kang et al., 2016). However, results of our study can be extended and are applicable to other operations.

We first extend a volume-averaged model for the CDI charging/discharging process based on mixed flow reactor type theory, first introduced by Biesheuvel et al. (2009). In addition to bulk electro-migration transport and EDL dynamics, our model also accounts for Faradaic losses at the electrode surfaces and considers non-zero potential of zero charge. We next simplify the model based on practical considerations, and derive reduced order models with closed-form *semi-analytical* and *analytical* solutions to evaluate desalination performance of CDI under various CC conditions. Specifically, we obtain expressions for cycle average and time variation of EDL efficiency, in addition to time variation of effluent concentration (Jande and Kim, 2013), and flow efficiency (Hawks et al., 2018), all under dynamic steady state (DSS) conditions. We identify the natural and CC forced responses of a CDI cell and its governing parameters, and demonstrate self-similar effluent concentration profiles across a wide range of time-average EDL and flow efficiencies. We performed an experimental study to validate our models and study the interplay between flow and EDL efficiencies in determining overall cycle efficiency and salt removal for CC CDI operation with varying voltage thresholds. To the best of our knowledge, our study is the first to identify self similarity in CDI desalination dynamics, i.e., identification of variables describing cell parameters and operational conditions which result in a unique temporal response for CDI cells. For the first time, we identify the unique value of these variables that give rise to optimum values of salt removal (given realistic constraints). This includes precisely quantifying trade-offs among salt removal, energy cost, and degree of desalination.

2. Theory

2.1 GCS-based dynamic model - Numerical

In this section, we describe a simple dynamic model in which we apply a mixed reactor type formulation of the form first used by Biesheuvel et al. (2009) for CDI cells. The model includes

electrical double layer (EDL) charge efficiency effects on salt removal and electro-migration effects. The model assumes a symmetric and binary, univalent salt with constant inlet concentration and neglects diffusive transport. Under these assumptions, mass balance for salt is given by

$$\forall \frac{dc}{dt} = Q\left(c_0 - c\right) - \Phi_{\text{salt}}, \tag{1}$$

where $\forall$ is the volume of flow compartment, c and c_0 are effluent and influent salt concentration respectively, Q is the volumetric flowrate, and Φ_{salt} is the cell-volume-averaged salt adsorption rate.

Charge transport from solution to the electrodes is modeled using the idea of an ohmic mass-transport layer. The potential drop across the mass transport layer, $\Delta\phi_{mtl}$, relates to electronic charging current density, J_{ch} (supplied by external power source) (with units of Amp/m^2) through a mass transport coefficient, g, as

$$J_{ch} = gcF\Delta\phi_{mtl} \tag{2}$$

where F is the Faraday's constant. Physically, g (units of μm/s) can be interpreted as inverse effective and approximate resistance of the solution within the cell volume.

Further, we use a Gouy-Chapman-Stern (GCS) EDL model and assume that the electrode pairs have the same area and EDL structure (except for equal but opposite sign in the electrode potential). In the GCS model (Zhao et al., 2010), the ionic surface charge density of EDL, σ, is given by

$$\sigma = 4\lambda_D c \sinh\left(\frac{\Delta\phi_d}{2}\right), \tag{3}$$

where, $\lambda_D = \left(8\pi c N_{av}\lambda_B\right)^{-1/2}$ is the Debye length, N_{av} is the Avogadro's number, $\lambda_B = e^2/\left(4\pi\varepsilon kT\right)$ is the Bjerrum length, and $\Delta\phi_d$ is the potential drop across the diffuse layer. In addition, w, the number of ions removed per unit internal electrode area, a, is given by

$$w = 8\lambda_D c \sinh^2\left(\frac{\Delta\phi_d}{4}\right) \tag{4}$$

The potential drop in the Stern layer, $\Delta\phi_{st}$, is related to the surface charge density as

$$\sigma F = c_{st}\left(\Delta\phi_{st} V_t\right), \tag{5}$$

where c_{st} is the specific Stern layer capacity (per internal electrode area) and V_t is the thermal voltage (used to obtain non-dimensional voltages $\Delta\phi_{mtl}$, $\Delta\phi_d$ and $\Delta\phi_{st}$). We define the total capacitive voltage difference in the CDI cell circuit, $\Delta\phi_{cap}$, which is distributed between the Stern layer and the diffuse layer at the two electrodes as

$$\Delta\phi_{cap} = 2\left(\Delta\phi_d + \Delta\phi_{st}\right). \tag{6}$$

Unlike the model of Biesheuvel et al. (2009), we will here consider two modifications to the mixed reactor type formulation. First, in addition to the ohmic mass transport layer, we consider an external resistance for the CDI cell which accounts for resistance due to material, wiring, and contacts.

Second and importantly, we here consider effects of coulombic efficiency due to leakage currents. Coulombic efficiency is defined as the ratio of applied instantaneous electric current to

the rate of adsorption of ionic charge into EDLs. These two charge per time quantities differ because charge is consumed by Faradaic charge-transfer reactions (often described as leakage current). The instantaneous Coulombic efficiency λ_c is defined as the ratio of ionic current density to the applied electronic current density $\left(\lambda_c = J_{ion} / J_{ch}\right)$. The ionic current density which can contribute toward salt removal, J_{ion}, can therefore be written as

$$J_{ion} = J_{ch} - J_l = \lambda_c J_{ch} \tag{7}$$

where J_l is the voltage dependent leakage current density. This leakage is typically estimated using a Butler-Volmer (Biesheuvel et al., 2011) or Tafel (Qu et al., 2016) equation. In our work, for simplicity, we will account for such Faradaic losses using an effective, cycle-averaged value for Coulombic efficiency (see Eq. (26) and Hawks et al. (2018)), obtained from experiments.

In CDI, electronic charge at electrode surfaces is balanced by both attraction of counter-ions and repulsion of co-ions (Biesheuvel, 2009; Cohen et al., 2011). At low potentials across EDLs and for symmetric electrolytes, the attraction and repulsion of ions is approximately equal at each electrode and so accumulated charge results in no removal of salt (defined as anion and cation pairs). Hence, we define a differential EDL charge efficiency λ_{dl} as the fraction of ionic current density which contributes toward salt removal as

$$\lambda_{dl} = F\frac{J_{\text{salt}}}{J_{ion}} = F\frac{J_{\text{salt}}}{\lambda_c J_{ch}} = \frac{dw}{d\sigma} = \tanh\left(\frac{\Delta\phi_d}{2}\right). \tag{8}$$

Note that our definition of differential EDL charge efficiency in Eq. (8) accounts for Faradaic losses, unlike the formulation in Biesheuvel et al. (2009). Eq. (8) also assumes that the time scale

associated with charge redistribution in the EDL is much smaller than that of concentration changes in the bulk.

Hence, the salt adsorption rate in Eq. (1) is related to the ionic current density through differential EDL charge and Columbic efficiencies as

$$\Phi_{\text{salt}} = AJ_{\text{salt}} = AJ_{ion}\lambda_{dl} / F = AJ_{ch}\lambda_c\lambda_{dl} / F \,, \tag{9}$$

where J_{salt} is the salt removal flux (units of mol/m^2-s), and A is the projected electrode area.

We next account for an effective non-zero potential of zero charge V_{PZC} due to the presence of native charges on the electrodes, since a significant, non-zero value of V_{PZC} can affect desalination performance of the CDI cell (Avraham et al., 2011). The external cell voltage V_{cell} is distributed among the resistive $\left(V_{res}\right)$ and capacitive $\left(V_{cap}\right)$ potentials, and V_{PZC}, as

$$V_{cell} = \left[IR + 2V_t\Delta\phi_{mtl}\right] + \left[2V_t\left(\Delta\phi_d + \Delta\phi_{st}\right)\right] + V_{PZC} = V_{res} + V_{cap} + V_{PZC} \,, \tag{10}$$

where $I = J_{ch}A$ is current supplied by the external power source. Finally, the rate of change of charge density at the electrodes is determined by the ionic current density to the double layer as

$$\frac{d\left(\sigma Fa/2\right)}{dt} = AJ_{ion} \,. \tag{11}$$

Eqs. (1) - (11) close our model for CDI operation and form a dynamical system which couples salt removal and charge transfer mechanisms. This constitutes two coupled ordinary differential equations (ODE) (Eqs. (1) and (11)) for respectively effluent concentration and charge which we solve numerically. We will hereafter refer to this as the *numerical* model.

2.2 Simplified model with time varying EDL efficiency – Semi-analytical

194 Here we consider reduction of the model of the previous section for DSS condition and CC
195 operation so that we can more easily explore the self similarities in response and dynamics. Our
196 goal is to identify specific combinations of CDI cell and operational parameters which result in a
197 unique dynamic response. We will refer to these combinations as variables required for
198 similarity. Further, we will show that fixing these combinations of variables ensures that many
199 effluent concentration versus time responses of many different cells and operations collapse to
200 the same solution; which we call self similarity in the response.

201 To this end, first, we rewrite the salt conservation Eq. (1) in terms of $\Delta c = c_0 - c$ as,

202
$$\underbrace{\frac{d\left(\Delta c\right)}{d\left(t/\tau\right)}}_{\text{Natural response}} + \Delta c = \underbrace{\frac{I\Lambda(t/\tau)}{FQ}}_{\text{Forcing function}} \tag{12}$$

203 where $\tau = \forall / Q$ represents the residence time scale and parentheses indicate "a function of".
204 The left-hand side captures the natural response dynamics, and the right-hand side represents a
205 forcing function (here CC operation). The dynamic charge efficiency $\Lambda(t/\tau)$ in Eq. (12), can be
206 written as a product of Coulombic and differential EDL efficiencies, as,

207
$$\Lambda(t/\tau) = \lambda_{dl}(t/\tau)\lambda_c(t/\tau) \ . \tag{13}$$

208 As a simplification, we will assume like Hawks et al. (2018) that the Coulombic efficiency can
209 be approximated by an effective constant value, i.e., $\lambda_c\left(t/\tau\right) \approx \lambda_c$. This effective value reflects
210 Faradaic type losses through the entire charge and discharge cycle (see Eq. (26) and SI Section
211 S1 for further discussion).

212 To provide a simplified approximation of $\lambda_{dl}(t/\tau)$ and couple the external applied current to salt
213 transport, we treat the electrical response of the CDI cell using a nonlinear resistive and

capacitive circuit which is mathematically equivalent to the dynamic GCS model discussed in Section 2.1 (see SI Section S1 for complete discussion). We assume that the effective series resistance does not change significantly during a cycle, as typical of CDI operation (e.g. see Hemmatifar et al., 2016). Further, we assume that the total diffuse (C_d), Stern (C_{st}) and equivalent (C_{eq}) capacitances are nearly constant during a CC operation, and are related by

$$\frac{1}{C_{eq}} = \frac{1}{C_d} + \frac{1}{C_{st}} \ . \tag{14}$$

Using Eq. (14), for DSS operation, we derive the EDL efficiency during the charging phase as,

$$\lambda_{dl}\left(t/\tau\right) \approx \tanh\left[\frac{\forall}{2V_t C_d}\frac{It}{Q\tau} + \frac{C_{eq}}{2V_t C_d}\left(V_{\min} - V_{PZC} + IR_{eq}\right)\right], \tag{15}$$

and for the discharge phase, we obtain

$$\lambda_{dl}\left(t/\tau\right) \approx \tanh\left[\frac{-\forall}{2V_t C_d}\frac{It}{Q\tau} + \frac{C_{eq}}{2V_t C_d}\left(V_{\max} - V_{PZC} - IR_{eq}\right)\right] . \tag{16}$$

where $V_{\min}$ and $V_{\max}$ are the minimum and maximum external cell voltages, and R_{eq} is the effective series resistance. In Eqs. (15) and (16), $t = 0$ corresponds to the start of the charging and discharging, respectively. We present further details around this derivation and estimation of the capacitances in the SI Section S2. We benchmarked the current reduced order model with the more complete numerical model described in Section 2.1 (see SI Section S2). Eqs. (12)-(16) represent a closed form model for effluent concentration for CC operation of CDI under DSS conditions. For this model, the CDI cell parameters are C_{eq}, R_{eq} , C_{st}, and V_{PZC}, and the operational parameters are Q, I, $V_{\min}$ and $V_{\max}$.

The model presented in this section constitutes a reduction of the two coupled ODEs of the preceding section, to a single ODE for effluent concentration Δc (Eq. (12)). This simple ODE model predicts that the effluent concentration and that the behavior will be self-similar given the following variables: (i) constant values of the flowrate-to-current ratio Q/I, (ii) time dynamics normalized by the residence (flow) time scale, i.e., t/τ, and (iii) equal values of modified low and high voltage values of the form $V_{low}\left(=V_{\min}-V_{PZC}+IR_{eq}\right)$ and $V_{high}\left(=V_{\max}-V_{PZC}-IR_{eq}\right)$, respectively. We refer to (i), (ii), and (iii) as the three variables which result in self-similar dynamic response of CC operation of a CDI cell. In the SI (Section S6.5), we mention a few other studies (Hawks et al., 2018; Hemmatifar et al., 2016; Johnson and Newman, 1971; Qu et al., 2018a) who have touched on some of these variables, but have not identified the set required for unique responses.

Finally, although the model described here results in a single ODE for Δc in time (Eq. (12)), we cannot find an analytical expression for $\Delta c(t)$. Eqs. (12)-(16) need to be solved numerically and hence, we refer to this reduced order model with time varying EDL efficiency as a *semi-analytical model*.

2.3 Simplified model with effective cycle EDL efficiency – Analytical

We here explore a further simplification of our model for CC operation which can be used to obtain a closed-form analytical expression for effluent concentration versus time for full CDI operation over charge and discharge cycles. Using an approach similar to Jande and Kim (2013), and Hawks et al. (2018), we assume a constant effective value of EDL efficiency $\bar{\lambda}_{dl}$. This

assumption enables an analytical solution to Eq. (12) using an ad-hoc value for $\overline{\lambda}_{dl}$. Under this assumption, Eq. (12) becomes

$$\frac{d(\Delta c)}{d(t/\tau)} + \Delta c = \frac{I\lambda_c\overline{\lambda}_{dl}}{FQ} \tag{17}$$

Instead of choosing an ad-hoc value for $\overline{\lambda}_{dl}$ as done in previous works (e.g., from curve fitting, or assuming $\overline{\lambda}_{dl}=1$), we choose $\overline{\lambda}_{dl}$ to be equal to the time average EDL efficiency during cyclic operation. To close our model in Eq. (17), we average Eqs. (15) and (16) in time to derive the time-average EDL efficiency during an entire charge and discharge cycle as,

$$\overline{\lambda}_{dl}(t_{ch}) = \overline{\lambda}_{dl}(t_{disch}) = \frac{\log\left[\cosh(\alpha_{\max})\right] - \log\left[\cosh(\alpha_{\min})\right]}{\alpha_{\max} - \alpha_{\min}} = \overline{\lambda}_{dl}\ , \tag{18}$$

where $\overline{\lambda}_{dl}(t_{ch})$ and $\overline{\lambda}_{dl}(t_{disch})$ denote the average differential EDL efficiency during the charging and discharging phases, and $\alpha_{\max} = \left(1-\frac{C_{eq}}{C_{st}}\right)\left[\frac{V_{\max} - V_{PZC} - IR_{eq}}{2V_t}\right]$, and $\alpha_{\min} = \left(1-\frac{C_{eq}}{C_{st}}\right)\left[\frac{V_{\min} - V_{PZC} + IR_{eq}}{2V_t}\right]$. In Eq. (18), the charging and discharging time can be estimated from the RC circuit analogy (see SI Sections S1 and S2). For charging a capacitor with capacitance C_{eq} using a current I, and operated within a voltage window of ΔV, the charging time is given by $C_{eq}\,\Delta V / I$. Thus, we obtain the charging/discharging time in Eq. (18) as,

$$\frac{t_{ch}}{\tau} \approx \frac{t_{disch}}{\tau} \approx \frac{C_{eq}}{\forall}\left(\frac{Q}{I}\right)\left[\left(V_{\max} - V_{PZC} - IR_{eq}\right) - \left(V_{\min} - V_{PZC} + IR_{eq}\right)\right] = \frac{C_{eq}}{\forall}\left(\frac{Q}{I}\right)\Delta V \tag{19}$$

where $\Delta V = V_{high} - V_{low}$, and we have assumed that λ_c is close to unity. Eq. (18) represents a closed-form algebraic expression for the effective differential EDL efficiency in a cycle resulting in salt removal and regeneration under CC operation. The expression (18) is particularly useful in highlighting key non-dimensional parameters in CDI cell operation. These are the ratio of the reduced operational voltages $V_{high} = V_{\max} - V_{PZC} - IR_{eq}$ and $V_{low} = V_{\min} - V_{PZC} + IR_{eq}$ to the thermal voltage, and the ratio of the Stern capacitance to the equivalent capacitance. Further, Eq. (18) also predicts that the average EDL efficiency in a cycle is strongly dependent on the reduced operational voltages, i.e., $\bar{\lambda}_{dl} = \bar{\lambda}_{dl}\left(V_{low}, V_{high}\right)$ and only weakly dependent on current or flowrate.

The closed-form analytical solution of Eq. (17) which predicts the variation in effluent concentration versus time for CC operation is

$$\Delta c(t) = \underbrace{\frac{I\bar{\lambda}_{dl}\lambda_c}{FQ}\left(1-e^{-t/\tau}\right)}_{\text{Forced response}} + \underbrace{\Delta c(0)e^{-t/\tau}}_{\text{Natural resposne}} . \tag{20}$$

where $\bar{\lambda}_{dl}$ is given by Eq. (18). Note that when DSS is reached, typically the natural response has decayed sufficiently, so only the forced response is observed.

Finally, using Eq. (20) under DSS, we evaluate the cycle efficiency Λ_{cycle}, defined as ratio of moles of salt removed as measured at the effluent to the input electrical charge in moles. We show in SI Section S3 that the cycle efficiency can be derived as

$$\Lambda_{cycle}\left(V_{low}, V_{high}, \frac{Q}{I}\right) = \frac{\text{Salt removed per cycle (in moles)}}{\text{Charge input per cycle (in moles)}} \approx \bar{\lambda}_{dl}\left(V_{low}, V_{high}\right)\lambda_{fl}\left(\Delta V, \frac{Q}{I}\right)\lambda_c \tag{21}$$

where λ_{fl} is the flow efficiency (see Hawks et al., 2018), which, for the CC operation considered here is given by

$$\lambda_{fl}\left(t_{ch}\right)=1-\frac{2}{\left(\frac{t_{ch}}{\tau}\right)}\log\left[\frac{2\exp\left(\frac{t_{ch}}{\tau}\right)}{1+\exp\left(\frac{t_{ch}}{\tau}\right)}\right]. \quad (22)$$

Physically, flow efficiency estimates the amount of salt removal as measured in the effluent stream relative to the true salt trapped at the electrodes. Flow inefficiencies arise from an insufficient volume of feed solution flowed during charging or discharging. From Eqs. (19) and (22), flow efficiency depends on the effective voltage thresholds and flowrate-to-current ratio (c.f. Eq. (21)). We choose here not to model Coulombic efficiency λ_c in Eq. (21) in detail, and instead concentrate in a regime where Faraday losses are kept to a low value by judicious choice of $V_{\max}$ (see also Section S6 of SI).

Eqs. (18)-(22) is our *analytical model.* Model parameters are the cell properties C_{eq}, R_{eq}, C_{st}, and V_{PZC}, and the operational parameters which are Q, I, $V_{\min}$, and $V_{\max}$. Note that the three similarity variables derived from the *semi-analytical* model of Section 2.2 also ensure self-similarity in the current *analytical* model (c.f. Eq. (20)). In SI Section S4, we discuss further implications of the *semi-analytical* and *analytical* models on predicting desalination dynamics, efficiencies, and total salt removal under DSS. We also discuss the rationale behind the choice of models we use in Section 4, when we compare models with experiments.

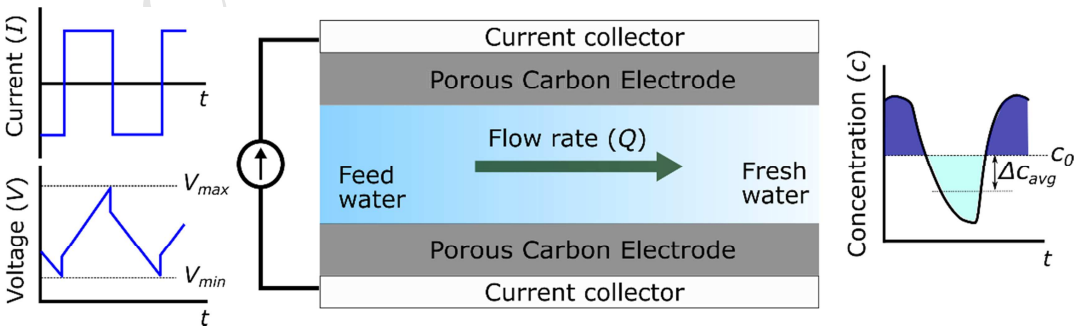

Figure 1: Schematic of a typical flow between capacitive deionization (fbCDI) cell. We highlight three operational parameters, namely, (i) current (*I*), (ii) voltage (*V*), and (iii) flowrate (*Q*), which affect the throughput, energy consumption, and salt removal (e.g. Δc_{avg}) performance of the system. The schematic's three sections are analogous to the input (left) and output (right) of the system (middle).

2.4 Performance metrics

We here define three performance metrics for a CDI cell and use these to explore system performance and tradeoffs between throughput and energy consumption, given realistic levels of salt reduction.

First, we describe the productivity (Prod) defined as the ratio of the feed processed rate to the total cross-section area of the electrode is

$$\text{Prod}\,[\text{L/m}^2/\text{h}] = \frac{V_{desal}}{t_{cycle} A}\,, \tag{23}$$

where V_{desal} is the volume of desalinated solution (in L) produced per cycle, t_{cycle} is the total cycle duration (in h), and A is the total electrode cross-section area (in m^2). The duration of desalination, t_{desal} is defined by the total duration when the effluent concentration is less than the feed (i.e., when $c < c_0$). Hence, the volume of feed solution processed during t_{desal} comprises the desalinated volume V_{desal}. The remainder volume (V_{brine}) processed during the cycle results in concentrated brine solution (corresponding to cycle time when $c > c_0$) at the effluent. Hence, water recovery (WR) is given by $\text{WR} = V_{desal} / (V_{brine} + V_{desal})$.

Second, we use volumetric energy cost (VEC) defined as the net energy spent in a charging-discharging cycle per unit volume of fresh water produced as

$$\mathrm{VEC\ [kWh/m^3]} = \frac{\oint VI\ dt}{3.6E6 \times V_{desal}}, \tag{24}$$

where the integration is performed for a complete charge-discharge cycle and V_{desal} has units of m^3.

Third, we evaluate salt removal as Δc_{avg}, defined as the average reduction in the salt concentration in the desalinated volume compared to the feed solution where

$$\Delta c_{avg}\,[\mathrm{mM}] = \frac{\int_{t|(c_0-c)>0} Q(c_0 - c)\ dt}{V_{desal}}. \tag{25}$$

Under DSS operation, if Faradaic losses are minimal, then CC charging and discharging times are nearly equal. To quantify such losses, we will estimate an average Coulombic efficiency, λ_c for a CC charge-discharge cycle as

$$\lambda_c = \frac{\text{recovered electronic charge}}{\text{input electronic charge}} = \frac{It_{disch}}{It_{ch}} = \frac{t_{disch}}{t_{ch}} \tag{26}$$

where t_{ch} and t_{disch} are the time spent in electrically charging the cell (at current I) and discharging the cell (at current $-I$), respectively.

3. Materials and Methods

3.1 CDI cell design

We fabricated and assembled an fbCDI cell using the radial-flow architecture described by Hemmatifar et al. (2016) and Zhao et al. (2013a). Five pairs of activated carbon electrodes (Materials & Methods, PACMM 203, Irvine, CA) with 5.6 cm diameter, 300 µm thickness, and total dry mass of 2.7 g were stacked between 5 cm diameter, 130 µm thick titanium sheets which acted as current collectors (total of six sheets). We used two 250 µm thick non-conductive polypropylene circular meshes (McMaster-Carr, Los Angeles, CA) between each electrode pair as spacers; these were cut with a slightly larger (~5 mm) diameter than electrodes and current collectors to prevent electrical short circuits. We estimate an effective spacer volume of 4.4 ml, with a porosity of 71%. This assembly was housed inside a CNC-machined acrylic clamshell structure and sealed with O-ring gaskets and fasteners. We compressed the entire assembly using C-clamps to lower the electrode-current collector contact resistance (see Qu et al., 2015 for effect of compression on contact resistance in CDI).

3.2 Experimental methods and model parameters extraction

The experimental setup consisted of the fbCDI cell, a peristaltic pump (Watson Marlow 120U/DV, Falmouth, Cornwall, UK), a 3 L reservoir filled with 20 mM potassium chloride (KCl) solution, a sourcemeter (Keithley 2400, Cleveland, OH), and a flow-through conductivity sensor (eDAQ, Denistone East, Australia) close to the cell outlet. We used KCl to approximate a binary, univalent and symmetric solution and circulated the solution in a closed loop with a 3 L reservoir. We estimate less than 1% change in reservoir concentration based on adsorption capacity of our cell, and thus approximate influent concentration as constant.

The resistance and capacitance of our (entire, assembled) cell were characterized using electrochemical impedance spectroscopy (EIS), cyclic voltammetry (CV), and simple galvanostatic charging (see SI Section S5 for EIS and CV data using a potentiostat/galvanostat

(Gamry Instruments, Warminster, PA, USA). We estimated effective capacitance values from the slope of voltage versus time data for constant current (CC) experiments using $C_{eq} = I/(dV/dt)$. For effective resistance estimates, we used the ohmic voltage drop $|\Delta V|_{I\to -I}$ during current reversal for CC operation at discharge, given by $|\Delta V|_{I\to -I} = 2IR_{eq}$. Thus, we estimated differential capacitances C_{eq} of 37.2 ± 1.8 F and an effective series resistance R_{eq} of 1.55 ± 0.28 Ohms, for 20 mM KCl. These estimates were confirmed using CV and EIS measurements (see SI sections S5 and S6.3 for further details on procedures used for model parameters extraction). For the Stern capacitance C_{st}, we estimated an optimal value that best fitted the dynamic effluent concentration data and obtained $C_{st}\left(=c_{st}a/2\right)$ of 41.6 ± 1.3 F (equivalent to 44 F/cm^3) for all data presented in this work. We observed ionic repulsion effects (Gao et al., 2015) at low voltages up to 0.3 V, and we corrected for this in our models by subtracting $V_{PZC} \sim 0.3$ V from the cell voltage when comparing model with experimental data throughout this work. To determine the mixed reactor volume $\forall$, we used an exponential fit to the natural response of our cell similar to Hawks et al. (2018) (see Section 4.1) and estimated $\forall = 4.5\pm0.2$ ml. Further, we performed constant current (CC) operation experiments using pre-defined voltage thresholds, and did not directly fix water recovery (WR). For all our CC experiments reported in this work, we had a WR of 50-55%.

4. Results

4.1 Similarity in natural response – open circuit flush following stop flow charging

We first look at the natural response of a CDI cell corresponding to an operation wherein $I(t) = 0$ and $\Delta c(0) \neq 0$. Physically, this operation is equivalent to an open circuit flush subsequent to a stopped-flow charging or discharging. The natural response presented here is

also reflected in the initial transients observed in the effluent concentration (before reaching DSS) during cycling operation with some forcing function (current or voltage). From Eq. (20), the natural response of the system is given by

$$\Delta c(t) = \Delta c(0)\exp(-t/\tau)\ , \tag{27}$$

where $\tau = \forall / Q$ is the flow residence time. Eq. (27) shows that in the absence of electric current (or any other forcing function), the difference between effluent and feed concentrations decays as a first order exponent in time.

Figs. 2a and 2b show raw effluent concentration data versus time after charging the CDI cell. Prior to t = 0, the cell was charged at stopped-flow condition with a constant current of 0.1 A for cell voltage windows of 0-0.8 V and 0-0.6 V, respectively. The result is two different initial conditions, $\Delta c(0)$. The effluent concentration (response of the system) is then plotted for each $\Delta c(0)$ and for an open circuit flush at four flowrates between 4.5 to 12 ml/min. Note the wide range of temporal dynamics. In Fig. 2c, we combine all effluent concentration reduction data from Figs. 2a and 2b and simply normalize time by the corresponding residence time τ. The horizontal alignment of the 8 different curves shows the value of this temporal normalization. To determine the cell volume (a constant for all cases) used in the definition of τ, we use raw experimental data and fit an exponential variation for the effluent concentration with time (Hawks et al., 2018) in the advection-dominated region (for $t/\tau > 1$). The inset of Fig. 2c shows the estimated residence time extracted for each of the four flushing flowrates and for each of the two initial conditions. The inset curve is strongly linear with a slope equal to a constant cell volume $\forall$ of $4.5(\pm 0.2)$ ml. This cell-geometry-specific value collapses the time scale of all responses across all flow rates and initial conditions (c.f. 8 operations of Fig. 2c). Further, the

extracted value for the mixed reactor volume (the cell volume participating in desalination in our fbCDI cell) is very close to the effective spacer volume of 4.4 ml as expected (c.f. Section 3.1). For a similar cell-volume characterization for an fteCDI system, refer to Hawks et al. (2018).

The effluent concentration is measured downstream, and so the initial step change in concentration is dispersed in a manner consistent with the assumption of mixed reactor volume. This dispersion effect is similar for both values of $\Delta c(0)$ and most pronounced for times less than a single residence time. Importantly, note that all the effluent concentration measurements corresponding to the same initial condition collapse onto the same curve (both in the dispersion-dominated and advection-dominated regions) when plotted against time normalized by the appropriate residence time. This results in unique effluent dynamics observed in the natural response of CDI. The figure therefore highlights the self-similarity of the natural response observed for the CDI cell for equal values of initial amount of salt removed $(\Delta c(0))$. This natural response is independent of the shape or intensity of the forcing function used to achieve the initial condition $\Delta c(0)$ (e.g., CC or constant voltage operation), and can be interpreted as the step input response of the CDI cell as a dynamic linear system with a single input (which determines $\Delta c(0)$) and output $(\Delta c(t))$. We note here that the only time scale governing the natural response (as a result of fluid flow) is the flow residence time. For any forced response (due to time varying voltage/current as in Section 4.2) coupled with fluid flow, CDI dynamics is influenced by both (i) flow residence time τ, and (ii) electrical *RC* time. An example of this coupling is readily apparent from Eq. (20) for a constant current forcing.

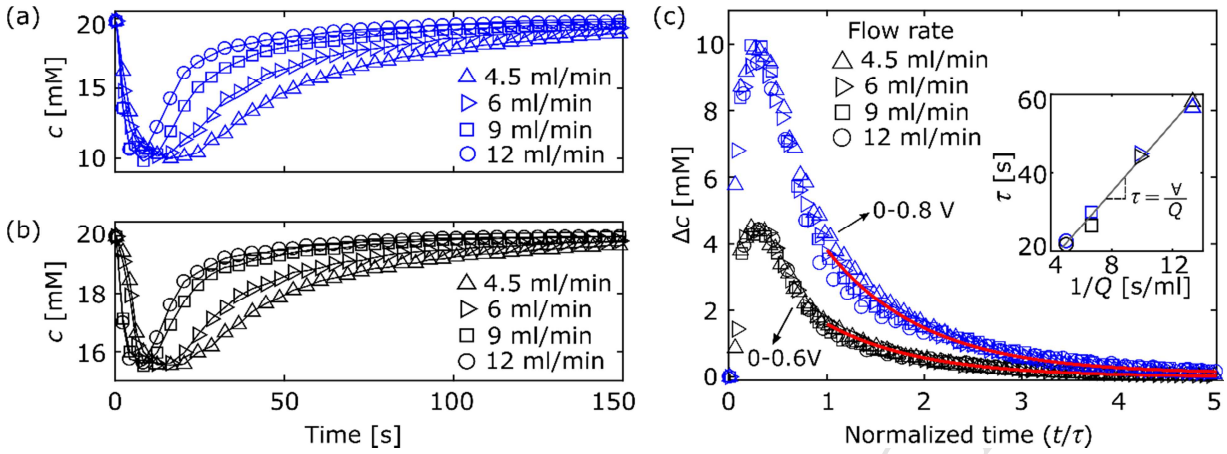

Figure 2: Measured effluent concentration versus time during an open circuit flush (following constant current charging at 100 mA) at 4.5, 6, 9, and 12 ml/min and for two cases of CC charging: (a) between 0-0.8 V (blue symbols), and (b) between 0-0.6 V (black symbols). (c) Effluent concentration reduction curves for cases (a) and (b) are plotted versus normalized time. Time is normalized by the residence time scale $(\tau = \forall / Q)$. Note that cases (a) and (b) each collapse onto a single curve, as indicated by the model. After an initial transient associated with dispersion effects for flow exiting the cell, the curves collapse to the exponential decay predicted by model (solid red curves). Inset in Fig. 2c presents the residence time (obtained from an exponential fit to the data; see Section 4.1) versus inverse flowrate for the same conditions as in cases (a) and (b), and shows a linear fit whose slope is the determined by the characteristic cell volume.

4.2 Similarity in time dynamics of CDI salt removal for constant current forcing function

We here explore a range of operations with varying current, flowrate and voltage thresholds to study self-similarity in CC CDI operations. We hypothesize that operations with the same flowrate-to-current ratio Q / I, and same effective voltage thresholds $V_{low}\left(= V_{\min} - V_{PZC} + IR_{eq}\right)$

441 and $V_{high}\left(=V_{\max}-V_{PZC}-IR_{eq}\right)$, have similar effluent concentration variation with normalized
442 time, t/τ. To study our hypothesis, we operated at three flowrate and current values but fixed
443 Q/I ratio as shown in Figs. 3a-c. Further, we adjusted the cell's operating voltage window by
444 varying $V_{\min}$ and $V_{\max}$ for different current values (for an effective resistance of 1.55 Ohms; see
445 SI Section S6 for more details) to ensure the same effective voltage thresholds V_{low} and V_{high}.
446 Results in Figs. 3a and 3b correspond to the same effective voltage thresholds, but different
447 Q/I. In Figs. 3b and 3c, we keep the same Q/I ratio but change the voltage threshold by
448 changing V_{low} (for the same V_{high}). In each case, we also compare the experimental results with
449 predictions from the *semi-analytical* model with time varying EDL efficiency. For all cases, we
450 used values of C_{eq} = 37.2 F and R_{eq} = 1.55 Ohms and C_{st} = 41.2 F in the model. The insets of
451 Figs. 3a-c show the raw, unscaled time variation of the effluent concentration for flowrates
452 which span 3 to 9 ml/min and current values of 50 to 100 mA, and varying cell voltage
453 thresholds. Operations which satisfy the self-similarity variables are grouped together in each of
454 Figs. 3a-c. In each subfigure, the insets show the wide range of absolute (unscaled, raw)
455 temporal dynamics of the effluent.

456 When time is normalized by the residence-time scale in Figures 3a-3c, there is a unique temporal
457 dynamic variation of effluent concentration vs. normalized time (i.e. a collapse onto the same
458 curve) across the cases which specifically preserve the similarity variables. This collapse
459 highlights the unique dynamics of self-similar operations. Note also that the normalized charging
460 and discharging durations are equal for operations which preserve similarity. Equal normalized
461 charging time during self-similar operations is well predicted by Eq. (19), resulting in the same

number of cell volumes flowed and thus the *same flow efficiency* (see also Section S6.1 and Table S1 of the SI).

In Table S1 of the SI, we report the average EDL efficiency at DSS for the experimental data in Fig. 3. For each of the three cases, we estimated the cycle effective EDL efficiency as follows. We divide the experimentally measured cycle efficiency (Eqn. (21)) by the product of predicted flow efficiency (Eq. (22)) and the measured Coulombic efficiency (Eqn. (26)), $\overline{\lambda}_{dl} = \Lambda_{cycle} / \left(\lambda_{fl} \lambda_c \right)$. This estimate yields nearly identical values of $\overline{\lambda}_{dl}$ for each self-similar case. For example, Figs. 3a, 3b and 3c each show self-similar operations (at three Q/I values each) and the corresponding EDL efficiencies for each of these self-similar operations are (0.7, 0.72, 0.75), (0.73, 0.76, 0.77), and (0.42, 0.41, 0.4) (see SI Table S1 and its discussion). This comparison is not an absolute confirmation of model accuracy but shows that self-similar operations yield consistent and nearly *identical values of the effective EDL efficiency*.

The average EDL efficiency values for Figs. 3a and 3b are nearly equal. Note also that the average EDL efficiency decreased from ~0.74 in Figs. 3a and 3b to 0.41 in Fig. 3c when the effective voltage thresholds $\left(V_{low}, V_{high} \right)$ changed from 0.25-0.65 V to -0.15-0.65 V, respectively. This is consistent with our model prediction that the average EDL in a cycle is mainly determined by the effective voltage thresholds (c.f. Eq. (18) and discussion, also Table S1 of SI).

Since self-similar operations have same flow and average EDL efficiencies, we hypothesize that, for minimal Faradaic losses, the cycle efficiency Λ_{cycle} (equal to the product of the efficiencies $\overline{\lambda}_{dl}$, λ_{fl} and λ_c as per Eq. (21)) is also equal across self-similar operations. This hypothesis is supported by our *analytical* model and by analysis of the experimental data (see cycle efficiency

values in SI Table S1). We caution the reader that this result holds true when we operate at moderate to high flowrates so the effects of diffusion are not significant, and in conditions where Faradaic losses are minimal. In all our operations presented in Fig. 3, the measured Coulombic efficiencies are high, > 90%.

A corollary to the above discussion is that self-similar operations also result in similar absolute values of average salt removal per cycle Δc_{avg} (Eq. (28)), because such operations have the same Q/I and Λ_{cycle}. This observation implies that a CDI user can choose among non-unique operation modes (e.g. flowrates and current) to achieve a single desired Δc_{avg} while meeting other constraints (such as a fixed values of $V_{\max}$ or $V_{\min}$ which respectively mitigate Faraday losses or operation at low $\overline{\lambda}_{dl}$). In other words, there exists some surface of equal concentration reduction Δc_{avg} in the operational parameter space of flowrate, current, and voltage thresholds. Lastly, note that Productivity and VEC may vary significantly under self-similar operation (see SI Table S1 for data), as these are explicit functions of both the flowrate and current as shown in Eqs. (29) and (30). In particular, VEC scales as I^2/Q while the Prod scales as Q (see Eqs. (29) and (30)).

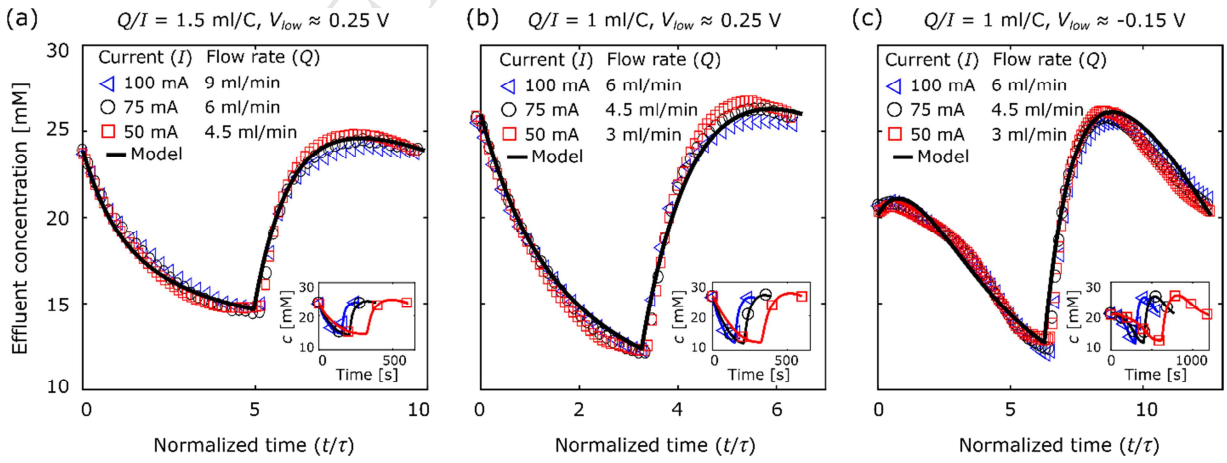

Figure 3: Measured effluent concentration versus normalized time is shown for (a) three cases of Q/I = 1.5 ml/C with current values of 50, 75 and 100 mA, and flowrates of 4.5, 6 and 9 ml/min respectively, between V_{low} = 0.25 V and V_{high} = 0.65 V, (b) three cases of Q/I = 1 ml/C with current values of 50, 75 and 100 mA, and flowrates of 3, 4.5 and 6 ml/min respectively, between V_{low} = 0.25 V and V_{high} = 0.65 V, (c) the same current and flowrates as in (b), but with V_{low} = -0.15 V and V_{high} = 0.65 V (larger voltage window). Experimental data are shown with symbols, and the semi-analytical model with time varying differential EDL efficiency (refer to Section 2.2) is shown with a solid line. The insets for (a)-(c) show the unscaled, raw time variation of effluent concentration corresponding to the conditions of the main plot. Results show strong self-similarity in time dynamics of salt removal under constant current CDI operation with equal values of Q/I, $V_{low}\left(=V_{\min}-V_{PZC}+IR_{eq}\right)$, and $V_{high}\left(=V_{\max}-V_{PZC}-IR_{eq}\right)$.

4.3 Average-EDL efficiency and flow efficiency have opposite trends for variations in voltage thresholds

We here explore the effects of changing voltage thresholds for CC operation on the flow, average EDL, and cycle efficiencies. Previous studies have suggested higher $V_{\min}$ can overall improve the dynamic cycle efficiencies by avoiding low EDL efficiency, λ_{dl} due to low $\Delta\phi_d$ (Kim et al., 2015). However, existing studies have not analyzed the effect of changing voltage thresholds on the flow, EDL, and cycle efficiencies simultaneously. We here show that this more complete view leads to an optimal voltage window that maximizes salt removal for the same Productivity and VEC.

519 In Fig. 4, we show data from two sets of CC charge/discharge experiments (symbols) and the
520 analytical model results (solid curves) with V_{max} threshold of 1 V and flowrate of 9 ml/min. In
521 Fig. 4a, the current is 100 mA and V_{min} varies between 0 to 0.6 V. In Fig 4b, the current is 50
522 mA and V_{min} varies between 0 to 0.7 V. For the model calculations, we use a value C_{st} = 41.8 F
523 and 42.8 F for Figs. 4a and 4b, respectively, and the same values of C_{eq} and R_{eq} mentioned
524 earlier (c.f. Section 4.2). To ensure a fair and accurate comparison, the cycle efficiency for the
525 model predictions is corrected by multiplying it with the average experimental Coulombic
526 efficiency.

527 Both Figs. 4a and 4b show low average EDL efficiency, $\bar{\lambda}_{dl}$ at small V_{min} values since a
528 significant portion of the cycle time is spent at low $\Delta\phi_d$. Higher V_{min} values always correspond
529 to higher $\bar{\lambda}_{dl}$. However, flow efficiency suffers at high V_{min} threshold values since this shortens
530 cycle times relative to τ and limits our ability to extract treated water from the cell, lowering λ_{fl}
531 . This trade-off between the average EDL and flow efficiencies results in a maximum cycle
532 efficiency at a V_{min} where the average EDL and flow efficiencies are nearly equal. This is
533 clearly shown by the measurements and matching predictions shown in Fig. 4.

534 We chose to plot Figs. 4a and 4b at the same flow rate with fixed V_{max} and varying V_{min} to
535 highlight the effect of varying current. The average EDL efficiency $\bar{\lambda}_{dl}$ is almost equal for the
536 same V_{min} (and V_{max}) for the 50 and 100 mA cases. Note also the consistently higher values for
537 flow efficiency λ_{fl} as current is decreased from 100 to 50 mA. Note also how the optimum
538 value of cycle efficiency (the product of $\bar{\lambda}_{dl}$ and λ_{fl}) shifts to values of higher V_{min}. This is due
539 to the relation between each of $\bar{\lambda}_{dl}$ and λ_{fl} with operational parameters. On one hand, lower

currents imply improved flow efficiency because of more cell volumes flowed prior to reaching the constant V_{max} limit. Flowing more volumes at lower current also implies that the region of rapid drop of λ_{fl} moves to higher values of V_{min}. On the other hand, for fixed V_{min} (and V_{max}), $\overline{\lambda}_{dl}$ does not change significantly with current since $\overline{\lambda}_{dl}$ depends mainly on the voltage dropped across the capacitive elements, given by $V_{low}\left(=V_{min}-V_{PZC}+IR_{eq}\right)$, and $V_{high}\left(=V_{max}-V_{PZC}-IR_{eq}\right)$, and does not explicitly depend on the current or flow rate (c.f. Sections 2.2 and 2.3). The net effect is an increased optimum value of V_{min} to achieve the proper trade-off between flowing enough volumes and maintaining potentials significantly greater than the thermal potential across the capacitive elements.

Moreover, we here specifically chose conditions (e.g., sufficiently low V_{max} = 1 V and maximum current of 100 mA) to achieve high cycle average Coulombic efficiencies of 97% and 90% for 100 and 50 mA cases, respectively. Such operation is likely of most practical interest and highlights the trade-off between $\overline{\lambda}_{dl}$ and λ_{fl}. We also hypothesize that for self-similar operations with a fixed voltage window difference, i.e., same $V_{high}-V_{low}$, increasing the lower voltage threshold primarily increases $\overline{\lambda}_{dl}$ (to near unity) for the same λ_{fl}. Lastly, we note that the values of average EDL efficiencies in Fig. 4 are slightly lower than that reported in literature (e.g. (Kim et al., 2015; Zhao et al., 2010)). We hypothesize this is because of our non-zero potential of zero charge (V_{PZC} ~ 0.3 V), which adversely affects salt removal performance and average EDL efficiency especially at cell voltages below V_{PZC} (see SI S6.4 for further discussion).

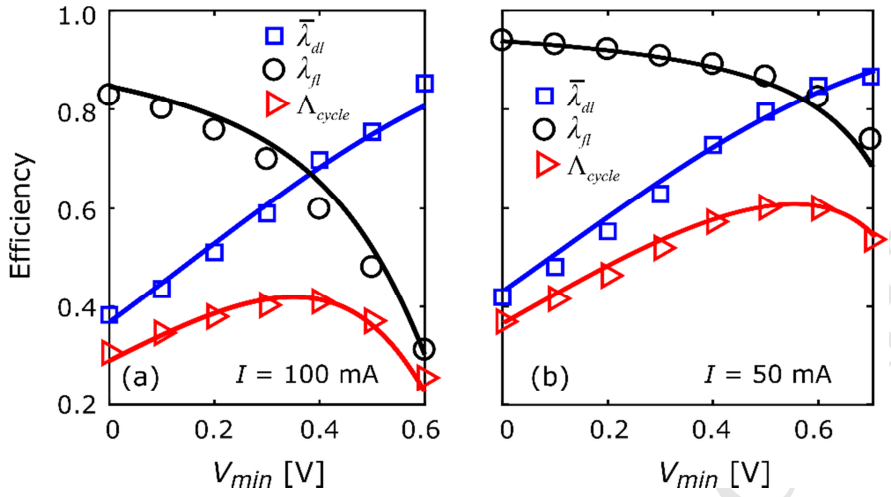

559

560 Figure 4: Measured cycle efficiency Λ_{cycle} (red triangles), estimated average-EDL efficiency $\bar{\lambda}_{dl}$
561 (blue squares), and flow efficiency λ_{fl} (black circles) versus minimum voltage ($V_{\min}$) for a
562 constant current CDI operation with (a) I = 100 mA, and (b) I = 50 mA. The maximum voltage (
563 $V_{\max}$) is 1 V and the flowrate is 9 ml/min for both cases. Symbols represent experimental data
564 and predictions from the analytical model with constant differential EDL efficiency (c.f. Section
565 2.3) are shown with solid lines. EDL efficiency losses dominate at low $V_{\min}$, as only a small
566 portion of electric charge is used for salt removal. At relatively high $V_{\min}$, the volume pumped
567 through the cell is insufficient to remove treated water, resulting in low flow efficiency. The
568 trade-off leads to a maximum in the cycle efficiency versus $V_{\min}$ curves.

569 **4.4 Changing voltage thresholds affects salt removal significantly, but energy and**
570 **throughput metrics are almost constant**

571 We explored the effect of voltage thresholds on CDI performance metrics. Fig. 5 shows the
572 variation of Δc_{avg}, Prod, and VEC each versus increasing $V_{\min}$ for the same operational
573 conditions as in Fig. 4. A comparison of Figs. 4 and 5a demonstrates how concentration

reduction Δc_{avg} follows the same trend as to cycle efficiency; as $V_{\min}$ increases, Δc_{avg} increases, reaches a maximum value, and then decreases. The reason for this correlation and trend is best expressed by the following identity:

$$\Delta c_{avg} = \frac{I \Lambda_{cycle}}{FQ} \ . \tag{28}$$

Hence, for equal flowrate-to-current ratio Q/I, Δc_{avg} and Λ_{cycle} are directly proportional and reach a maximum simultaneously (e.g. while changing voltage thresholds).

We next study the effect of changing flowrate-to-current ratio Q/I on Δc_{avg}. In Fig. 5a, as Q/I increases (here we show for constant flowrate and changing current), in general we observe that Δc_{avg} decreases. However, from Figs. 4a and 4b, cycle efficiency Λ_{cycle} increases with higher Q/I; a trend opposite to that of Δc_{avg} for changing Q/I. We explored this opposite trend shown by Λ_{cycle} and Δc_{avg} with changing Q/I in further detail in Section 4.5.

Fig. 5b shows that Prod and VEC are only weak functions of voltage window for fixed current and flowrate conditions. These trends are best interpreted using two approximate relations. If we assume a Coulombic efficiency of approximately unity (i.e. negligible parasitic Faraday losses), we can simplify the metrics (Eqns. (24) and (23)) as follows:

$$\text{VEC} = \frac{2I^2 R_{eq}}{Q} \tag{29}$$

$$\text{Prod} = \frac{Q}{2A} \tag{30}$$

Hence, to a first approximation, for a fixed current and flowrate, the Prod and VEC are independent of voltage window. In our experiments at 100 mA CC operation (Fig 5b), Coulombic efficiency has only 3% variations (96-99%). For the 50 mA case, Coulombic efficiency varies 10% (85-95%) with higher values at lower $V_{\min}$ (see SI Section S6.2 for data). Hence in Fig. 5b, Prod and VEC are approximately constant for the 100 mA cases, and both metrics show a slight increase with increasing $V_{\min}$ for 50 mA. Note the dashed lines in Fig. 5b are model predictions assuming a unity Coulombic efficiency. For VEC, the difference between model prediction and data is the result of energy loss due to parasitic reactions, which is more prominent at the 50 mA current. These results have critical consequences for CDI operation and quantification of CDI cell performance. For example, Fig. 5 shows how current can be varied to reach a desired trade-off between Prod and VEC; but if V_{min} is not simultaneously optimized (as per Figs. 4 and 5a) then Δc_{avg} can suffer enormously. Conversely, optimizing Δc_{avg} and VEC can be achieved by varying current and V_{min}; but mostly likely at the expense of low Prod.

In summary, the salt removal varies significantly and shows a pronounced maximum versus voltage threshold for a fixed flowrate-to-current. On the other hand, Prod and VEC are each a strong function of flowrate and current and depend only weakly on voltage thresholds. At low currents, there is less voltage dropped on series resistance and the cell spends greater time with a higher voltage on capacitive components, so that Coulombic losses dominate (see also Hemmatifar et al. (2016)).

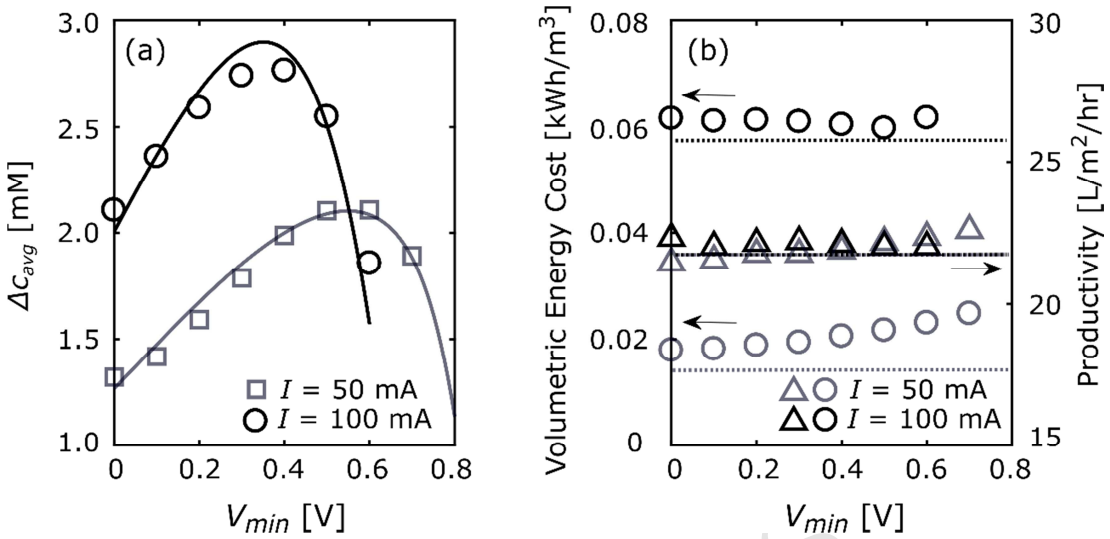

Figure 5: Measured values of CDI performance metrics and comparisons with model: (a) Absolute quantity of salt removal (Δc_{avg}), and (b) volumetric energy cost (VEC) and Productivity (Prod), versus minimum voltage (V_{min}) for constant current CDI operation. Maximum voltage (V_{max}) and flowrate are fixed at 1 V and 9 ml/min, and shown are results for currents, I of 50 mA (grey markers) and 100 mA (black markers). The experimental conditions are identical to those of Fig. 4. Results from the closed-form analytical model with constant differential EDL efficiency (refer to Section 2.3) are presented by solid lines in (a) and dashed lines in (b). At fixed flowrate, current, and V_{max}, the salt removal follows a trend identical to the cycle efficiency in Fig. 4 and attains a maximum value at the same V_{min}. In contrast, VEC and Prod are relatively constant with voltage window. At low current values, Coulombic losses become important, leading to a slight increase in the VEC at high V_{min} values.

4.5 Interplay among flowrate, current and voltage thresholds on CDI performance: Predictions from experimentally validated model

We here use the experimentally validated analytical model to study the interplay among current, flowrate, and voltage thresholds on efficiencies (Fig. 6a) and performance metrics (Fig. 6b). For

626 the cell parameters, we use extracted values of C_{eq} = 38.8 F, R_{eq} = 1.5 Ohms and C_{st} = 40.5 F
627 as determined from our preliminary experiments, and set V_{high} = 1 V. We consider the self-
628 similarity variables, Q/I and the effective voltage thresholds, V_{low} and V_{high} as discussed in
629 Section 4.2.

630 Fig. 6a shows contours of the cycle efficiency versus Q/I and voltage threshold, V_{low}. At a
631 fixed V_{low}, flow efficiency increases with Q/I ratio, while average EDL efficiency is relatively
632 constant (see Sections 2.3 and 4.2, and Eqs. (18) and (22)). This leads to an overall increase in
633 the cycle efficiency with increasing Q/I ratio. At a fixed Q/I, however, the flow efficiency
634 and average EDL efficiency respectively decreases and increase with increasing V_{low}. This leads
635 to an optimal lower voltage threshold $V_{low,opt}$ that maximizes cycle efficiency. This optimal lower
636 voltage increases as Q/I increases. So, for high cycle efficiency, we are driven to operate at
637 high Q/I and at the lower voltage threshold given by $V_{low,opt}$. Of course, these trends need to be
638 weighed against the requirement for sufficient salt removal $\left(\Delta c_{avg}\right)$ as discussed next.

639 Fig. 6b shows contours of salt removal, Δc_{avg} versus Q/I and voltage threshold, V_{low}. For fixed
640 Q/I, increasing V_{low} initially increases but then decreases salt removal in the same way as cycle
641 efficiency (see Fig. 6a, and refer to Section 4.4 and Eq. (28)). However, unlike cycle efficiency,
642 salt removal monotonically decreases with Q/I. Hence, a CDI cell user with a primary
643 objective of strong salt removal is driven to operate at low Q/I and at the optimal voltage
644 $V_{low,opt}$ (same optimum that maximizes cycle efficiency) for CC operation. However, at low
645 Q/I, Prod and VEC are each adversely affected. Recall from Eqs. (29) and (30) that high ratios

of Q/I imply respectively higher Prod and lower VEC but also lower degree of salt removal. Hence a user must properly consider the importance they attribute to Prod, salt removal, and VEC in determining CC operation. The key operational parameters available include flowrate, current, and voltage window(s) of operation.

Lastly, we emphasize that, in general, high cycle efficiencies are not necessarily correlated with high salt removal performance. Such a correlation holds only when the flowrate-to-current is fixed, and voltage thresholds are varied. We hypothesize that the trends discussed here regarding efficiencies and performance will be representative of CDI cells in practical use.

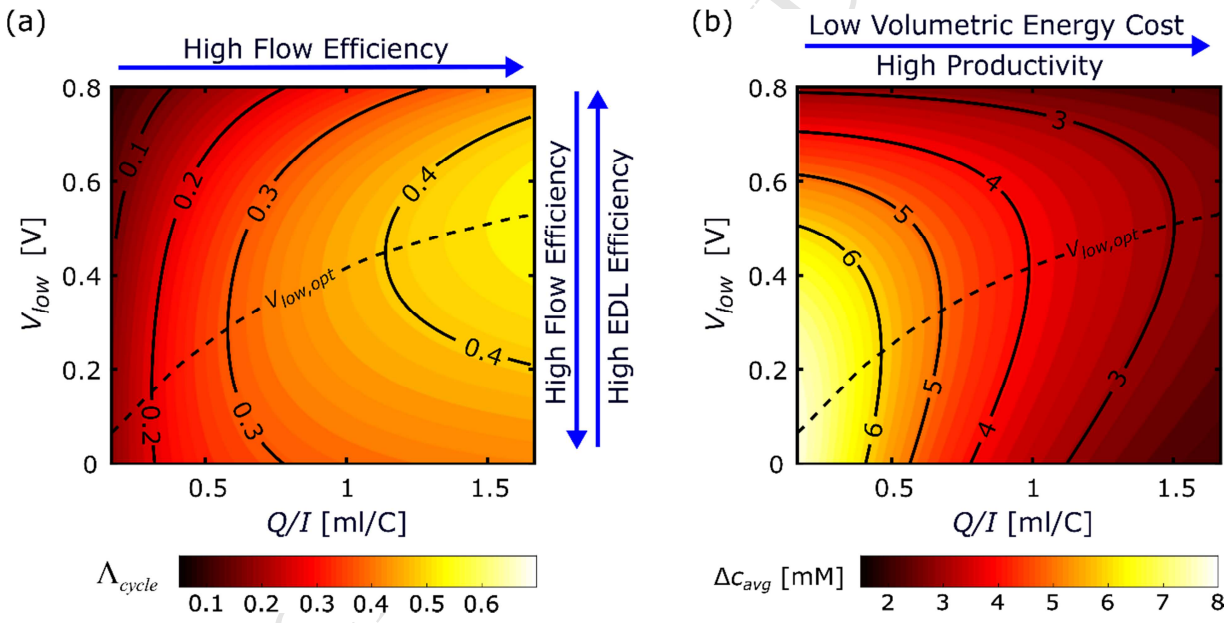

Figure 6: Predicted performance metrics for CC CDI operation based on experimentally validated model. Shown are contour plots of (a) cycle efficiency, and (b) salt removal (Δc_{avg}) versus flowrate-to-current ratio (Q/I) and the minimum voltage (V_{low}) based on the analytical model with constant differential EDL efficiency (refer to Section 2.3) for V_{high} = 1 V. Dashed lines in (a) and (b) indicate the optimal minimum voltage $V_{low,opt}$ for each value of Q/I ratio

660 which maximizes both cycle efficiency and salt removal (Δc_{avg}), simultaneously. Note cycle
661 efficiency increases while salt removal decreases with increasing Q/I. The arrows in (a) and (b)
662 indicate a monotonic (but not linear) trend of each quantity. Flow efficiency and average EDL
663 efficiency have opposite trends with changing V_{low}, and this results in an optimal voltage value
664 $V_{low,opt}$ which maximizes their product (= cycle efficiency). Higher Q/I results in better Prod
665 and lower VEC but lower average concentration reduction. This highlights the trade-off among
666 the performance metrics in CDI.

667 **5. Summary and Conclusions**

668 We developed several reduced order models based on a mixed reactor approximation which
669 describe the dynamics and performance of CDI systems. We concentrated on CC operation, but
670 an analogous approach can be used for other operational control methods. The first (numerical)
671 model includes the effects of bulk electromigration, EDL charge efficiency, Faradaic losses, and
672 non-zero potential of zero charge. This model results in basically two coupled ODEs in time for
673 respectively the effluent salt concentration and electrical charge on the electrodes, can be solved
674 numerically, and is a useful tool for benchmarking the other two models. The second (semi-
675 analytical) model further assumes a constant effective capacitance for the CDI cell and reduces
676 to a single ODE in time for the effluent concentration which yields insight into non-dimensional
677 parameters which govern operation and similarity. The third (analytical) model assumes an
678 effective (constant) value of EDL efficiency and yields closed-form algebraic expressions
679 describing dynamics of effluent concentration variation, and values of EDL and flow efficiencies
680 as a function of operational parameters. We used the second and third models to clearly identify
681 the natural and CC forced response of a CDI system, and describe parameters and dynamics

682 which lead to self-similar performance of CDI. This self-similar approach highlights the
683 interplay among flowrate, current, and voltage thresholds in CC CDI operation and performance.

684 We also performed an experimental study using a flow between CDI cell. We performed
685 preliminary experiments using galvanostatic charging and discharging, electrochemical
686 impedance spectroscopy, and cyclic voltammetry to extract three cell parameters for the model.
687 We fixed these cell parameters and validated the model across fairly wide variations of control
688 parameters. We showed that CC operations with same flowrate-to-current ratio, and reduced
689 effective voltage thresholds, exhibit similar effluent dynamics when time is normalized by the
690 residence time scale. We verified that the average EDL efficiency is a strong function of the
691 voltage thresholds, and only weakly depends on the current and flowrate, as predicted by the
692 analytical model. We also proposed and explored global performance metrics including cycle
693 efficiency, average (absolute) concentration reduction, productivity, and volumetric energy cost
694 (VEC). We showed that self-similar operations resulted in almost equal values of cycle
695 efficiency and average concentration reduction, while productivity and VEC depended explicitly
696 on flowrate and current. We used the validated model to explore a full performance map of
697 charge efficiency, average concentration reduction, productivity, and VEC, each as a function of
698 flowrate-to-current ratio and effective voltage thresholds. These show that higher values of
699 flowrate-to-current result in better cycle efficiency, throughput, and VEC, but poor average
700 concentration reduction. The comparison of these performance maps demonstrates the trade-off
701 among salt removal, throughput and VEC versus CC operation parameters.

702 **Acknowledgements**

703 We gratefully acknowledge funding from the California Energy Commission grant ECP-16-014.
704 Work at LLNL was performed under the auspices of the US DOE by LLNL under Contract DE-

AC52-07NA27344. A.R. gratefully acknowledges the support from the Bio-X Bowes Fellowship of Stanford University. A.H. gratefully acknowledges the support from the Stanford Graduate Fellowship program of Stanford University.

References

Avraham, E., Bouhadana, Y., Soffer, A., Aurbach, D., 2009. Limitation of Charge Efficiency in Capacitive Deionization. J. Electrochem. Soc. 156, P95. https://doi.org/10.1149/1.3115463

Avraham, E., Noked, M., Cohen, I., Soffer, A., Aurbach, D., 2011. The Dependence of the Desalination Performance in Capacitive Deionization Processes on the Electrodes PZC. J. Electrochem. Soc. 158, 168–173. https://doi.org/10.1149/2.078112jes

Biesheuvel, P.M., 2009. Thermodynamic cycle analysis for capacitive deionization. J. Colloid Interface Sci. 332, 258–264. https://doi.org/10.1016/j.jcis.2008.12.018

Biesheuvel, P.M., Bazant, M.Z., 2010. Nonlinear dynamics of capacitive charging and desalination by porous electrodes. Phys. Rev. E 81, 31502. https://doi.org/10.1103/PhysRevE.81.031502

Biesheuvel, P.M., Fu, Y., Bazant, M.Z., 2011. Diffuse charge and Faradaic reactions in porous electrodes. Phys. Rev. E 83, 61507. https://doi.org/10.1103/PhysRevE.83.061507

Biesheuvel, P.M., Limpt, B. Van, Wal, A. Van Der, 2009. Dynamic Adsorption / Desorption Process Model for Capacitive Deionization 5636–5640.

Cohen, I., Avraham, E., Noked, M., Soffer, A., Aurbach, D., 2011. Enhanced Charge Efficiency in Capacitive Deionization Achieved by Surface-Treated Electrodes and by Means of a Third Electrode. J. Phys. Chem. C 115, 19856–19863. https://doi.org/10.1021/jp206956a

726 Gao, X., Omosebi, A., Landon, J., Liu, K., 2015. Surface charge enhanced carbon electrodes for
727 stable and efficient capacitive deionization using inverted adsorption–desorption behavior.
728 Energy Environ. Sci. 8, 897–909. https://doi.org/10.1039/C4EE03172E

729 Guyes, E.N., Shocron, A.N., Simanovski, A., Biesheuvel, P.M., Suss, M.E., 2017. A one-
730 dimensional model for water desalination by flow-through electrode capacitive
731 deionization. Desalination 415, 8–13. https://doi.org/10.1016/J.DESAL.2017.03.013

732 Han, L., Karthikeyan, K.G., Gregory, K.B., 2015. Energy Consumption and Recovery in
733 Capacitive Deionization Using Nanoporous Activated Carbon Electrodes. J. Electrochem.
734 Soc. 162, E282–E288. https://doi.org/10.1149/2.0431512jes

735 Hawks, S.A., Knipe, J.M., Campbell, P.G., Loeb, C.K., Hubert, M.A., Santiago, J.G.,
736 Stadermann, M., 2018. Quantifying the flow efficiency in constant-current capacitive
737 deionization. Water Res. 129, 327–336. https://doi.org/10.1016/J.WATRES.2017.11.025

738 Hemmatifar, A., Palko, J.W., Stadermann, M., Santiago, J.G., 2016. Energy breakdown in
739 capacitive deionization. Water Res. 104, 303–311.
740 https://doi.org/10.1016/J.WATRES.2016.08.020

741 Hemmatifar, A., Stadermann, M., Santiago, J.G., 2015. Two-Dimensional Porous Electrode
742 Model for Capacitive Deionization. J. Phys. Chem. C 119, 24681–24694.
743 https://doi.org/10.1021/acs.jpcc.5b05847

744 Jande, Y.A.C., Kim, W.S., 2013. Desalination using capacitive deionization at constant current.
745 Desalination 329, 29–34. https://doi.org/10.1016/J.DESAL.2013.08.023

746 Johnson, A.M., Newman, J., 1971. Desalting by Means of Porous Carbon Electrodes. J.

747 Electrochem. Soc. 118, 510. https://doi.org/10.1149/1.2408094

748 Kang, J., Kim, T., Jo, K., Yoon, J., 2014. Comparison of salt adsorption capacity and energy
749 consumption between constant current and constant voltage operation in capacitive
750 deionization. DES 352, 52–57. https://doi.org/10.1016/j.desal.2014.08.009

751 Kang, J., Kim, T., Shin, H., Lee, J., Ha, J.I., Yoon, J., 2016. Direct energy recovery system for
752 membrane capacitive deionization. Desalination 398, 144–150.
753 https://doi.org/10.1016/j.desal.2016.07.025

754 Kim, T., Dykstra, J.E., Porada, S., van der Wal, A., Yoon, J., Biesheuvel, P.M., 2015. Enhanced
755 charge efficiency and reduced energy use in capacitive deionization by increasing the
756 discharge voltage. J. Colloid Interface Sci. 446, 317–326.
757 https://doi.org/10.1016/J.JCIS.2014.08.041

758 Kim, T., Yoon, J., 2014. CDI ragone plot as a functional tool to evaluate desalination
759 performance in capacitive deionization. RSC Adv. 5. https://doi.org/10.1039/C4RA11257A

760 Oren, Y., 2008. Capacitive deionization (CDI) for desalination and water treatment — past,
761 present and future (a review). Desalination 228, 10–29.
762 https://doi.org/https://doi.org/10.1016/j.desal.2007.08.005

763 Qu, Y., Baumann, T.F., Santiago, J.G., Stadermann, M., 2015. Characterization of Resistances of
764 a Capacitive Deionization System. Environ. Sci. Technol. 49, 9699–9706.
765 https://doi.org/10.1021/acs.est.5b02542

766 Qu, Y., Campbell, P.G., Gu, L., Knipe, J.M., Dzenitis, E., Santiago, J.G., Stadermann, M., 2016.
767 Energy consumption analysis of constant voltage and constant current operations in

768 capacitive deionization. Desalination 400, 18–24.
769 https://doi.org/10.1016/j.desal.2016.09.014

770 Qu, Y., Campbell, P.G., Hemmatifar, A., Knipe, J.M., Loeb, C.K., Reidy, J.J., Hubert, M.A.,
771 Stadermann, M., Santiago, J.G., 2018a. Charging and Transport Dynamics of a Flow-
772 Through Electrode Capacitive Deionization System. J. Phys. Chem. B acs.jpcb.7b09168.
773 https://doi.org/10.1021/acs.jpcb.7b09168

774 Qu, Y., Campbell, P.G., Hemmatifar, A., Knipe, J.M., Loeb, C.K., Reidy, J.J., Hubert, M.A.,
775 Stadermann, M., Santiago, J.G., 2018b. Charging and Transport Dynamics of a Flow-
776 Through Electrode Capacitive Deionization System. J. Phys. Chem. B 122, 240–249.
777 https://doi.org/10.1021/acs.jpcb.7b09168

778 Suss, M.E., Porada, S., Sun, X., Biesheuvel, P.M., Yoon, J., Presser, V., 2015. Water
779 desalination via capacitive deionization: what is it and what can we expect from it? Energy
780 Environ. Sci. 8. https://doi.org/10.1039/C5EE00519A

781 Wang, L., Lin, S., 2018. Intrinsic tradeoff between kinetic and energetic efficiencies in
782 membrane capacitive deionization. Water Res. 129, 394–401.
783 https://doi.org/10.1016/J.WATRES.2017.11.027

784 Zhao, R., Biesheuvel, P.M., Miedema, H., Bruning, H., Wal, A. Van Der, 2010. Charge
785 Efficiency: A Functional Tool to Probe the Double-Layer Structure Inside of Porous
786 Electrodes and Application in the Modeling of Capacitive Deionization 205–210.
787 https://doi.org/10.1021/jz900154h

788 Zhao, R., Porada, S., Biesheuvel, P.M., van der Wal, A., 2013. Energy consumption in
789 membrane capacitive deionization for different water recoveries and flow rates, and

comparison with reverse osmosis. Desalination 330, 35–41. https://doi.org/https://doi.org/10.1016/j.desal.2013.08.017

Zhao, R., Porada, S., Biesheuvel, P.M., van der Wal, A., 2013a. Energy consumption in membrane capacitive deionization for different water recoveries and flow rates, and comparison with reverse osmosis. Desalination 330, 35–41. https://doi.org/10.1016/J.DESAL.2013.08.017

Zhao, R., Satpradit, O., Rijnaarts, H.H.M., Biesheuvel, P.M., van der Wal, A., 2013b. Optimization of salt adsorption rate in membrane capacitive deionization. Water Res. 47. https://doi.org/10.1016/j.watres.2013.01.025

Highlights:

- Identified cell and operational variables which results in unique dynamic responses
- Developed reduced order models for CDI operation
- Demonstrated interplay between flow and EDL efficiencies in CC operation
- Identified optimal salt removal operation in CC CDI for realistic constraints
- Highlighted tradeoffs among salt removal, energy, and throughput performance